Article

Imaging viscous flow of the Dirac fluid in graphene

Check for updates

Mark J. H. Ku[1,2,3,14,15], Tony X. Zhou[1,4,15], Qing Li[1], Young J. Shin[1,5], Jing K. Shi[1], Claire Burch[6], Laurel E. Anderson[1], Andrew T. Pierce[1], Yonglong Xie[1,7], Assaf Hamo[1], Uri Vool[1,8], Huiliang Zhang[1,3], Francesco Casola[1,3], Takashi Taniguchi[9], Kenji Watanabe[9], Michael M. Fogler[10], Philip Kim[1,4]✉, Amir Yacoby[1,4]✉ & Ronald L. Walsworth[1,2,3,11,12,13]✉

The electron–hole plasma in charge-neutral graphene is predicted to realize a quantum critical system in which electrical transport features a universal hydrodynamic description, even at room temperature[1,2]. This quantum critical 'Dirac fluid' is expected to have a shear viscosity close to a minimum bound[3,4], with an interparticle scattering rate saturating[1] at the Planckian time, the shortest possible timescale for particles to relax. Although electrical transport measurements at finite carrier density are consistent with hydrodynamic electron flow in graphene[5–8], a clear demonstration of viscous flow at the charge-neutrality point remains elusive. Here we directly image viscous Dirac fluid flow in graphene at room temperature by measuring the associated stray magnetic field. Nanoscale magnetic imaging is performed using quantum spin magnetometers realized with nitrogen vacancy centres in diamond. Scanning single-spin and wide-field magnetometry reveal a parabolic Poiseuille profile for electron flow in a high-mobility graphene channel near the charge-neutrality point, establishing the viscous transport of the Dirac fluid. This measurement is in contrast to the conventional uniform flow profile imaged in a metallic conductor and also in a low-mobility graphene channel. Via combined imaging and transport measurements, we obtain viscosity and scattering rates, and observe that these quantities are comparable to the universal values expected at quantum criticality. This finding establishes a nearly ideal electron fluid in charge-neutral, high-mobility graphene at room temperature[4]. Our results will enable the study of hydrodynamic transport in quantum critical fluids relevant to strongly correlated electrons in high-temperature superconductors[9]. This work also highlights the capability of quantum spin magnetometers to probe correlated electronic phenomena at the nanoscale.

Understanding the electronic transport of strongly correlated quantum matter is a challenging problem given the highly entangled nature of interacting many-body systems. Nevertheless, many disparate correlated systems share universal features owing to quantum criticality. A paradigmatic example is the electron–hole plasma in high-mobility graphene at the charge-neutrality point (CNP), known as the Dirac fluid[4,10], which is expected to share universal features present in other quantum critical systems, even at room temperature[1]. First, particle–particle scattering occurs on the timescale[1] $\tau_{pp} \approx \tau_\hbar$, where the Planckian time $\tau_\hbar = \hbar/(k_B T)$ is the fastest timescale for entropy generation allowed by the uncertainty principle at temperature T ($\hbar$ is the reduced Planck's constant and k_B is the Boltzmann constant). Such a universal

quantum-critical scattering rate is observed for electron–hole systems in monolayer[11] and bilayer/trilayer graphene[12]. With a fast $\tau_{pp} \ll \tau_{mr}$, where τ_{mr} is the momentum-relaxation time, local equilibrium can be established. As a result, a simple, universal description of collective particle motion emerges in which electrical transport resembles that of hydrodynamic fluids. A quantum critical electron fluid involving a maximal 'Planckian' dissipative process is postulated to underlie the linear-T resistivity observed in the strange metal phase of high-temperature superconductors[9]. Second, as a result of Planckian-bounded dissipation, the Dirac fluid in graphene is expected to have a ratio of shear viscosity η to entropy density s that saturates at an 'ideal fluid' lower bound[2–4] $\eta/s \geq \hbar/(4\pi k_B)$.

[1]Department of Physics, Harvard University, Cambridge, MA, USA. [2]Quantum Technology Center, University of Maryland, College Park, MD, USA. [3]Harvard-Smithsonian Center for Astrophysics, Cambridge, MA, USA. [4]John A. Paulson School of Engineering and Applied Sciences, Harvard University, Cambridge, MA, USA. [5]Center for Functional Nanomaterials, Brookhaven National Laboratory, Upton, NY, USA. [6]Harvard College, Harvard University, Cambridge, MA, USA. [7]Department of Physics, Massachusetts Institute of Technology, Cambridge, MA, USA. [8]John Harvard Distinguished Science Fellows Program, Harvard University, Cambridge, MA, USA. [9]National Institute for Materials Science, Tsukuba, Japan. [10]Department of Physics, University of California, San Diego, La Jolla, CA, USA. [11]Center for Brain Science, Harvard University, Cambridge, MA, USA. [12]Department of Physics, University of Maryland, College Park, MD, USA. [13]Department of Electrical and Computer Engineering, University of Maryland, College Park, MD, USA. [14]Present address: Department of Physics and Astronomy, University of Delaware, Newark, DE, USA. [15]These authors contributed equally: Mark J. H. Ku, Tony X. Zhou. ✉e-mail: yacoby@g.harvard.edu; walsworth@umd.edu
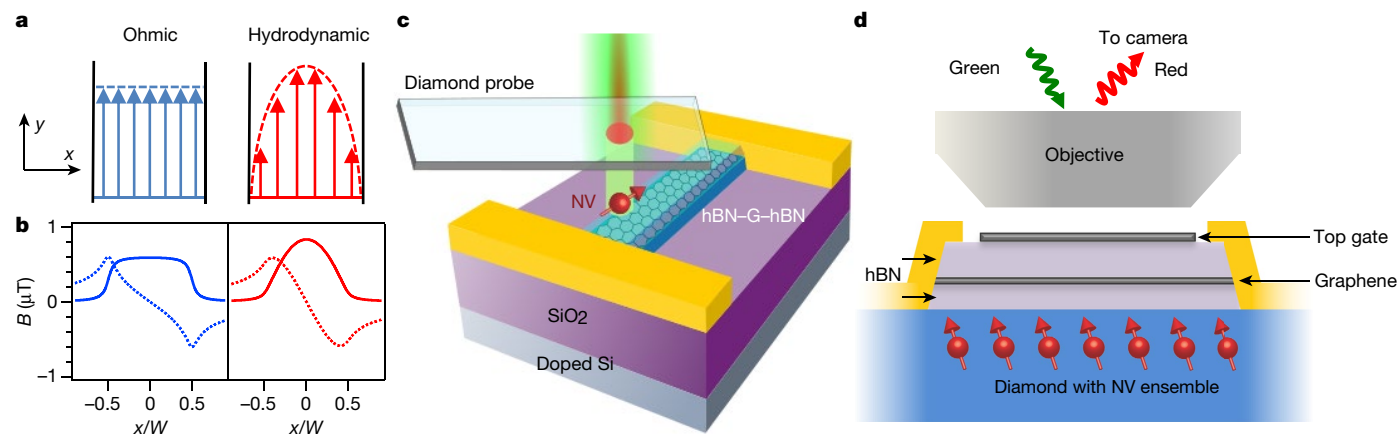
Fig. 1 | Probing viscous electronic transport via magnetic field imaging. Local current density J_y in a 2D conductor oriented along the y direction for conventional ohmic transport (left) and viscous Poiseuille flow (right). **b**, Magnetic field $B_x(x)$ (solid line) and $B_z(x)$ (dashed line) at $z = d$ generated by an electronic flow $J_y(x)$ in the y direction for ohmic (left) and viscous Poiseuille flow (right). Here the magnetic field profile is shown for a channel width $W = 1\,\mu m$, current $I = 1\,\mu A$ and stand-off distance $d = 50\,nm$. Hence, a quantum spin magnetometer located at $z = d$ from a 2D current distribution $\mathbf{J}$ probes the local current via sensing the local magnetic field $\mathbf{B}$ generated by $\mathbf{J}$. **c**, **d**, Magnetic field imaging modalities employed in this work. **c**, Scanning NV magnetometry with a diamond probe containing a single near-surface NV spin, excited by green light. NV red photoluminescence is collected by a confocal microscope. hBN-encapsulated graphene device (hBN–G–hBN) is fabricated on a SiO$_2$/doped Si substrate. Typical stand-off distance $\lesssim 50\,nm$ between NV and graphene. **d**, Wide-field magnetic imaging. An hBN-encapsulated graphene device with a graphite top gate is fabricated on a macroscopic diamond chip containing a high-density ensemble of near-surface NVs. Green excitation light is sent through an objective to illuminate the field of view. NV photoluminescence is collected by the same objective and imaged onto a camera with 420-nm 2D resolution.

Compared with the non-interacting particle case, hydrodynamic electron flow is expected to be dramatically modified owing to viscosity, for example, leading to vortices near a constriction and a parabolic velocity profile in a channel (known as Poiseuille flow)[2]. Signatures of such viscous electron flow have been observed in electrical transport[5–8,13,14], scanning gate measurements[15] and scanning single-electron transistor measurement of the Hall field[16]. However, experiments in graphene have so far been unable to provide information on whether viscous Dirac fluid flow occurs near the CNP[5–8,10,16]. Hydrodynamic transport applies to the velocity field $\mathbf{u}$, which is related to electrical current[17–19] via $\mathbf{J} = e(n_e - n_h)\mathbf{u} + \delta\mathbf{J}$. Here e is the electron charge, n_e (n_h) is the density of electrons (holes), and $\delta\mathbf{J}$ is an ohmic correction. At finite doping, $|n_e - n_h| > 0$ suppresses $\delta\mathbf{J}$ and hence the electrical current can reveal hydrodynamic transport. At the CNP, $n_e - n_h = 0$, additional coupling between $\mathbf{u}$ and $\mathbf{J}$ is needed for electrical current to manifest viscous flow. In theory, such coupling may arise from an applied magnetic field or thermoelectric effect, but has not been experimentally observed. Thus the question of whether there is viscous Dirac fluid flow near the CNP remains open.

Here we address this question by directly imaging the flow of the Dirac fluid at room temperature in a high-mobility graphene channel via measurement of the flow-induced stray magnetic field $\mathbf{B}$ using nitrogen vacancy (NV) centres in diamond[20]. Inside a conductor where the dominant scattering is momentum relaxing, for example, owing to impurities, phonons or Umklapp processes, the conventional ohmic transport of electrons in a channel exhibits a uniform current profile. In contrast, a hydrodynamic electron fluid can develop a parabolic (Poiseuille) current profile (Fig. 1a). For a two-dimensional (2D) current distribution $\mathbf{J}$, the inverse problem between $\mathbf{J}$ and $\mathbf{B}$ is unique[21]; therefore, measurement of $\mathbf{B}(x, y, z = d)$, where d is the sensor–source stand-off distance, reveals the local current flow (Fig. 1b). For our experiments, magnetic imaging of current flow is performed with two complementary modalities: (1) scanning probe microscopy using a single NV centre[22,23] (Fig. 1c); and (2) wide-field magnetic imaging with an ensemble of NVs[24] (Fig. 1d). We find clear experimental evidence for non-slip carrier flow at channel boundaries; and strong deviation from a flat current profile. These results are in stark contrast with otherwise similar measurements we performed on a conventional ohmic conductor and low-mobility graphene. Below we describe our experimental findings in detail and discuss them in light of existing theories.

We begin with scanning single-NV magnetic microscopy[22,25], which has spatial resolution $\lesssim 50\,nm$ (Methods). For the devices we interrogate, the dimension along which the electrical current flows (the y direction) is much longer than the device's narrow dimension (along the x direction). Therefore, we perform a 1D scan of the single NV probe across the width of the device W to measure the projective stray field along the NV axis $B_\parallel(x)$ (Fig. 2a–c), from which we obtain $J_y(x)$ and subsequently elucidate the presence of hydrodynamic flow.

As a benchmark, we first perform measurements on a thin palladium channel (Fig. 2a) and a low-mobility graphene device (Fig. 2b) in which disorder is intentionally introduced (Methods). Local current density can be reconstructed via inverting the Biot–Savart law and assuming the continuity equation $\nabla \cdot \mathbf{J} = 0$. The resulting current profiles $J_y(x)$ for the palladium channel and the low-mobility graphene device are shown in Fig. 2e. The current profiles show a clear hallmark of ohmic transport, with a near-uniform J_y that drops sharply at the edges $x/W = \pm 0.5$.

We next apply scanning NV magnetic microscopy to measure current profiles in high-quality graphene devices, with nanoscale resolution. A device consists of a hexagonal boron nitride (hBN)-encapsulated monolayer graphene on a standard SiO$_2$/doped Si substrate. The encapsulation ensures orders-of-magnitude increase in mobility and reduction in momentum-relaxing scattering, a necessary condition to enter the hydrodynamic regime. Unless otherwise noted, all references to graphene are for such high-quality, encapsulated samples. The measured $B_\parallel$ at the CNP is shown in Fig. 2c and the resulting current density is shown in Fig. 2e. The CNP is identified by a transport measurement of resistivity as a function of carrier density (Fig. 2d), as controlled by the gate voltage. In contrast to the ohmic profile seen in the palladium channel and the low-mobility graphene device, the current profile in the standard graphene device is distinctly parabolic and vanishes at the boundary within experimental uncertainty. Similar profiles are observed in four standard devices (Fig. 2f), three at small current (about 1 μA) and one at large current (20 μA, second profile from the left). While the profile of non-interacting electrons also develops curvature when the momentum-relaxation mean free path $l_{mr} = v_F\tau_{mr} \sim W$, where the Fermi velocity $v_F = 10^6\,m\,s^{-1}$, we rule out this ballistic transport
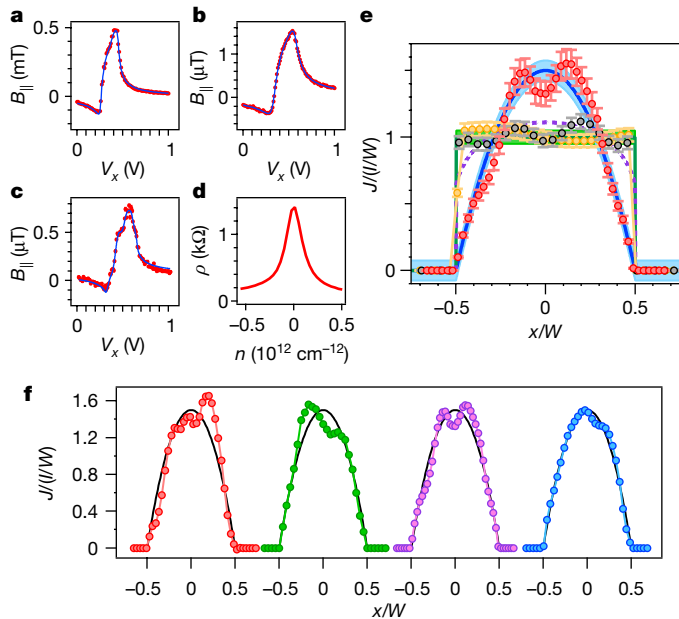
Fig. 2 | One-dimensional scanning NV microscopy of ohmic flow in a metallic channel and low-mobility graphene and viscous flow in hBN-encapsulated graphene at the CNP. a–c, Scanning magnetometry of the projective stray field $B_{\parallel}$ measured with the palladium channel (**a**), the low-mobility graphene device (**b**) and a standard (hBN-encapsulated) graphene device (**c**) at the CNP. The horizontal axis is the piezovoltage that drives the scanning probe in the x direction. The lines are $B_{\parallel}$ from reconstructed current density J_y. **d**, Transport measurement of resistivity ρ versus carrier density n for hBN-encapsulated graphene device, same as in **c**. The standard graphene device is set to the CNP by tuning the gate voltage to achieve maximal resistivity. Data for the palladium channel are measured with ODMR and a sourced current of 1 mA. Data for the low-mobility and standard graphene devices are measured with spin-echo a.c. magnetometry (The details of the measurement technique are described in Methods). A source–drain voltage V_{sd} = 50 mV is applied for the low-mobility device and 5.8 mV for the standard device. The width is 1 μm for the low-mobility and standard graphene devices and 800 nm for the palladium channel. The palladium channel is 30 nm thick and 100 μm long. All the graphene devices measured in this work have lengths ≥5 μm. For all devices, scanning magnetometry is performed at a y position near the mid-point along the length of the channel. For graphene devices, we ensure the y position of the scan is within 1 μm of the longitudinal mid-point via atomic force microscopy with the diamond probe. **e**, Reconstructed current density $J_y(x)$. J_y is normalized by the average charge carrier flux I/W, where $I = \int dx\, J_y(x)$ is the total flux and W is the width of the channel. The spatial coordinate x is normalized by W and centred on the channel. Red points, graphene at the CNP; grey points, palladium channel; orange points, low-mobility graphene. Error bars correspond to the relative deviation of J_y that generates $2\chi^2$, where χ^2 is the cost function. Blue (green) lines, ideal viscous (uniform) flow with 5% error band; purple dashed curve, current profile of non-interacting electrons with diffusive boundary condition and momentum-relaxing mean free path $l_{mr} = 0.625W$, which corresponds to the maximum possible curvature for a non-interacting flow (Supplementary Information). **f**, Current profile at the CNP from four different standard hBN-encapsulated graphene devices. Second profile from left is for current of 20 μA and is measured with ODMR, whereas other profiles have current ≤ 2 μA and are measured with spin-echo a.c. magnetometry.

scenario by noting the inconsistency of the current profile in this regime with measured profiles and a magneto-transport experiment (Methods). Instead, the measured profiles have a compelling match with a viscous flow profile. Furthermore, our data show that by turning on and off disorder, the current profile in graphene switches between uniform and parabolic. This result is consistent with a transition between disorder-dominated ohmic and collision-dominated hydrodynamic regimes. The consistency between experiment and theory

constitutes an observation of viscous Poiseuille flow of the Dirac fluid in room-temperature graphene.

In addition, the boundary condition for the electron fluid in graphene was not previously known[19]. Previous work that explored viscous flow in graphene (at finite doping) involved vortex backflow[5,7,8] and superballistic conductance across point contacts[6], but neither phenomenon requires a specific boundary condition. Our experimental finding that the current density vanishes at the channel edges identifies a no-slip boundary condition at room temperature. Recent theory work[26] enables an estimate of the slip length of about 80 nm << W at room temperature (Supplementary Information), consistent with the experimental observation. Note that past experimental work at reduced temperatures was not able to establish viscous current flow at the CNP and the boundary condition in graphene[5–8].

In all devices, we observe an isolated dip in the current profile, close to the centre of the graphene channel. While the nature of this current profile dip requires future investigation, we note that recombination is expected to play a role in the transport of electron–hole systems[27–29], leading to peaks in the current density associated with the edges of a flow in a channel[28,29]. This scenario is compatible with the experimental conditions in our devices (Methods).

The measurement described so far assumes uniformity of the system along the y direction as well as the continuity equation. As a complementary measurement, we perform wide-field 2D imaging of the vector magnetic field resulting from current in a graphene device, which allows us to map the electronic flow with minimal assumptions. The measurement is performed on an hBN-encapsulated graphene device with a graphite top gate (optical image in the inset of Fig. 3a) fabricated on diamond with a high-density ensemble of near-surface NV spins (Fig. 1d). Figure 3a shows the measured B_x and B_y as a function of position (x, y) in the graphene device. The resulting 2D vector current map is shown in Fig. 3b. The measured current density has a flow pattern with direction and magnitude that are consistent with how the current is sourced and drained. More quantitatively, this vector current map allows us to verify that the continuity equation $\nabla \cdot \mathbf{J} = 0$ holds (Supplementary Information). Furthermore, the measured net incoming current flux at the top of the device and the outgoing flux at the bottom-left side probe are both consistent with a source–drain current of 100 μA.

In Fig. 3c, we show a line-cut of the current density far away from the device drain, $J_y(x, y = 2.5\,\mu m)$. We can then compare the measured current density profile with calculated diffraction-limited profiles of uniform and viscous electron flow, for the same total current, 100 μA. As seen in Fig. 3c, the experimentally measured J_y profile at the CNP clearly deviates from uniform flow and matches well a parabolic Poiseuille profile. This result provides further confirmation of the observation of viscous Dirac fluid flow in room-temperature graphene.

We next investigate the carrier-density dependence of current profiles in graphene. Owing to photoinduced doping in back-gated encapsulated devices, a scanning measurement away from the CNP averages over a range of carrier densities (Supplementary Information). The top panel of Fig. 4a shows current profiles measured with the scanning NV magnetic microscope averaged over several different ranges of carrier densities. In all cases, the current profile is consistent with viscous flow. Similar observations are made with wide-field vector magnetic imaging. The top-gated graphene-on-diamond device is immune from photoinduced doping and allows NV measurements at a specified value of the carrier density[30]. The bottom panel of Fig. 4a shows diffraction-limited current profiles at several carrier densities up to 1.5×10^{12} cm^{-2}, all of which are consistent with a Poiseuille profile and hence viscous flow. While previous imaging work at T = 75 K and 150 K in a graphene channel with W = 4.7 μm has shown that electric transport moves away from the Poiseuille regime as carrier density increases[16], the insensitivity of the current profile to carrier density
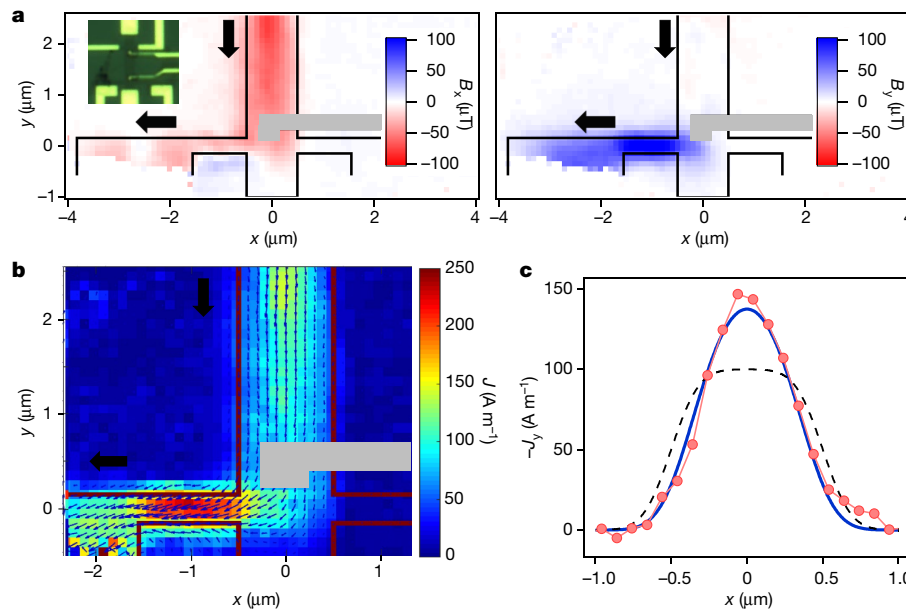
Fig. 3 | Wide-field magnetic imaging of viscous electron flow in graphene. **a**, The 2D spatial distribution of B_x (left) and B_y (right) measured by wide-field NV vector magnetometry, for a source–drain current of 100 µA and NV ensemble imager located in positive z direction. Inset: optical image of device channel $W = 1$ µm. Current is sourced from the top contact to the bottom-left contact. **b**, Vector (arrow) and amplitude (colour) plots of current density $\mathbf{J}(x,y)$ extracted from vector field measurement. In **a** and **b**, the grey outline denotes area covered by a metallic top-gate contact that obstructs light, and top/bottom left black arrows indicate the direction of the bias from the source/drain. **c**, Horizontal line-cut of **b** far away from drain, $J_y(x, y = 2.5$ µm$)$, measured at the CNP. Calculated diffraction-limited profiles of a uniform (black) and viscous (blue) flow are also shown.

observed here may be due to the much narrower channel used in our experiment (Methods).

To determine the kinematic viscosity v of the Dirac fluid and as a function of carrier density, we consider an electronic flow along the y direction in a 2D channel with $|x| \le W/2$, where W is the channel width. Evaluating the electronic Navier–Stokes equation[2], assuming a no-slip boundary condition $J_y(x = \pm W/2) = 0$, gives the following current density and conductivity[28,31]

$$J_y(x) = \frac{e^2 v_F \tau_{mr}}{\hbar} \sqrt{\frac{n}{\pi}} E\left(1 - \frac{\cosh(x/D_v)}{\cosh(W/(2D_v))}\right) \qquad (1)$$

$$\sigma = \frac{e^2 v_F \tau_{mr}}{\hbar} \sqrt{\frac{n}{\pi}} \left(1 - \frac{2D_v}{W} \tanh\left(\frac{W}{2D_v}\right)\right) \qquad (2)$$

Here E is the bias electrical field, n is the carrier density and the Gurzhi length $D_v \equiv \sqrt{v\tau_{mr}}$ is a characteristic length that determines the scale of viscous effects. In the limit $D_v \gg W$, J_y becomes the parabolic profile of ideal viscous flow, $J_y(x) = \frac{e^2 v_F}{2\hbar v} \sqrt{\frac{n}{\pi}} E\left(\left(\frac{W}{2}\right)^2 - x^2\right)$. As profiles with $D_v/W > 0.3$ are indistinguishable from an ideal viscous flow within experimental uncertainty, we estimate the lower bound on the Gurzhi length to be $0.3W$ for the profiles presented in this paper for 1-µm-wide channels. Accordingly, we then obtain bounds on v using equation (2) and the measured conductivity. Figure 4b shows values for v as a function of carrier density corresponding to $D_v/W = \infty$ and 0.3, which set the upper and lower bounds respectively for the Gurzhi length; as well as for $D_v/W = 0.5$, which provides the median value. Near the CNP, where thermal energy $k_B T$ becomes comparable to or exceeds the Fermi energy $E_F = \hbar v_F \sqrt{\pi n}$, the kinematic viscosity v for the Dirac fluid is extracted from our measurement using a carrier density n obtained from $E_F(n) = k_B T$. Away from the CNP, at relatively large carrier density, our experiment gives $v \approx 0.1$ m^2 s^{-1}, which is consistent with past transport measurements performed in graphene at finite doping[5,6]. We note that a recent calculation based on kinetic theory[17] compares very well

with both our experimental result for the kinematic viscosity v in the Dirac fluid, as well as present and past measurements at finite carrier density (Fig. 4b). Note that this good agreement with existing theory does not extend to measurements on a wider channel (Methods), for which l_{mr}/W is smaller and hence deviations from hydrodynamic behaviour may be expected, including, for example, discrepancies in D_v and v. For the narrow-channel (1 µm) results, we define the viscous scattering time as $\tau_v \equiv v/v_F^2$ and show the values of τ_v normalized by the Planckian time $\tau_\hbar$ on the right vertical axis of Fig. 4b. τ_v is not necessarily the same as the particle–particle scattering time τ_{pp}, but is expected to be the same order of magnitude. The results for the viscous scattering time are consistent with the expectation for a quantum critical system, where the Planckian time sets the scale for scattering. On the basis of our result and the quantum critical scattering time $\tau_{pp} = 5\tau_\hbar$ measured for a Dirac fluid[11], we estimate (Supplementary Information) $\tau_v \approx 1$–$3\tau_{pp}$.

Lastly, Fig. 4c shows the shear viscosity $\eta = nmv$ determined from our measurements, where $m = \hbar\sqrt{\pi n}/v_F$ is the carrier effective mass. The shear viscosity is normalized by the entropy density s_0 of neutral graphene at $T = 300$ K, which we determined from the calculation in ref. [4]. For an 'ideal fluid', this quantity reaches the conjectured lower bound $\eta/s = \hbar/(4\pi k_B) = 0.08\hbar/k_B$. Close to the CNP, we observe $\eta/s_0 \approx 0.3$–$0.8\hbar/k_B$, which lies between the theoretical value of $0.26\hbar/k_B$ for a Dirac fluid at 300 K from ref. [4] and an experimental estimate of about $10\hbar/k_B$ for a Dirac fluid at about 100 K from ref. [18]. We note that our value for η/s_0 near the CNP is comparable to the value of about $0.4\hbar/k_B$ obtained in cold atoms[32] and $\lesssim 0.5\hbar/k_B$ in quark gluon plasma[33]. Thus, our result adds a new data point for η/s in strongly interacting quantum matter, from a condensed-matter system, and highlights the trend of strongly interacting systems exhibiting η/s within an order of magnitude of the 'ideal fluid' lower bound.

The observation of viscous flow of the Dirac fluid in room-temperature, high-mobility graphene indicates a coupling between the velocity field and electric current at the CNP, which enables current measurements to reveal the underlying hydrodynamic transport. Theoretically, it is known that a number of potential mechanisms may lead to such
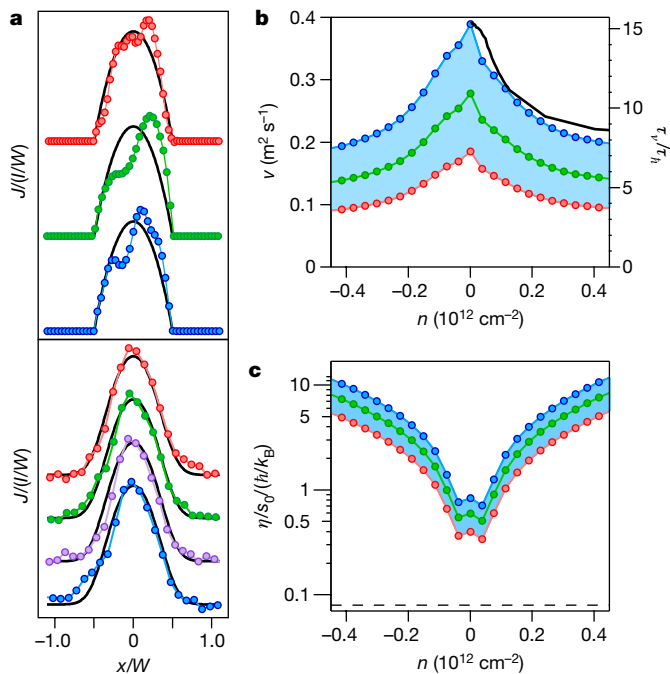
Fig. 4 | Electron hydrodynamics in graphene near the CNP. a, Normalized current density $J_y/(I/W)$ as a function of x/W, where I is the total charge carrier flux and W is the graphene device width. Top panel: data obtained from scanning NV probe magnetometry. Data points are for the CNP (top), averaged over carrier density $n = 0.1 \times 10^{12} - 0.3 \times 10^{12}\,cm^{-2}$ (middle) and averaged over $n = 0.3 \times 10^{12} - 1.5 \times 10^{12}\,cm^{-2}$ (bottom). Solid curve is for calculated ideal viscous flow. Bottom panel: data obtained from wide-field NV vector magnetic imaging. Data points from top to bottom correspond to the CNP and $n = 0.17 \times 10^{12}$, $0.85 \times 10^{12}\,cm^{-2}$ and $1.50 \times 10^{12}\,cm^{-2}$, respectively. Solid curve is for calculated diffraction-limited ideal viscous flow. Observations with both modalities are consistent with viscous flow at the CNP, as well as at finite carrier density as previously established[5–8]. **b**, Bounds on kinematic viscosity ν obtained from equation (2) and measured conductivity. $D_\nu/W = \infty$, 0.3 and 0.5 set the Gurzhi length upper bound, lower bound and median, as given by the blue, red and green dots, respectively. The blue shading indicates the values of ν within the bounds. Shown on right vertical axis is the corresponding viscous scattering time τ_ν normalized by the Planckian time $\tau_\hbar$. The black curve is the kinetic theory calculation at $T = 300\,K$ with no adjustable parameters from ref. [17]. **c**, The ratio of shear viscosity η to s_0, where s_0 is entropy density at the CNP calculated in ref. [4]. η/s_0 is normalized by $\hbar/k_B$. Upper bound, lower bound and median are given by the blue, red and green dots, respectively, while the blue shading indicates the values enclosed within the bounds. The black dashed line is the 'ideal fluid' lower bound[3] $1/(4\pi)$.

coupling, including an applied magnetic field, as in our experiment, and/or a thermoelectric effect; future work will be required to elucidate these and other potential sources of velocity–current coupling. The role of recombination in the transport of the Dirac fluid is another topic that deserves further exploration. Beyond viscous flow, electronic turbulence may also be explored via magnetic imaging experiments, as one can tune the Reynolds number by increasing the current and observe the evolution of the time-averaged flow profile from laminar to turbulent. Lastly, our magnetic imaging techniques can be deployed for nanoscale study of an increasing number of materials manifesting viscous electronic flow, as well as other correlated electronic phenomena, such as topological transport in the quantum spin Hall effect.

1. Müller, M. & Sachdev, S. Collective cyclotron motion of the relativistic plasma in graphene. *Phys. Rev. B* **78**, 115419 (2008).
2. Levitov, L. & Falkovich, G. Electron viscosity, current vortices and negative nonlocal resistance in graphene. *Nat. Phys.* **12**, 672–676 (2016).
3. Kovtun, P. K., Son, D. T. & Starinets, A. O. Viscosity in strongly interacting quantum field theories from black hole physics. *Phys. Rev. Lett.* **94**, 111601 (2005).
4. Müller, M., Schmalian, J. & Fritz, L. Graphene: a nearly perfect fluid. *Phys. Rev. Lett.* **103**, 025301 (2009).
5. Bandurin, D. A. et al. Negative local resistance caused by viscous electron backflow in graphene. *Science* **351**, 1055–1058 (2016).
6. Krishna Kumar, R. et al. Superballistic flow of viscous electron fluid through graphene constrictions. *Nat. Phys.* **13**, 1182–1185 (2017).
7. Bandurin, D. A. et al. Fluidity onset in graphene. *Nat. Commun.* **9**, 4533 (2018).
8. Berdyugin, A. I. et al. Measuring Hall viscosity of graphene's electron fluid. *Science* **364**, 162–165 (2019).
9. Zaanen, J. Planckian dissipation, minimal viscosity and the transport in cuprate strange metals. *SciPost Phys.* **6**, 061 (2019).
10. Crossno, J. et al. Observation of the Dirac fluid and the breakdown of the Wiedemann–Franz law in graphene. *Science* **351**, 1058–1061 (2016).
11. Gallagher, P. et al. Quantum-critical conductivity of the Dirac fluid in graphene. *Science* **364**, 158–162 (2019).
12. Nam, Y., Ki, D.-K., Soler-Delgado, D. & Morpurgo, A. F. Electron–hole collision limited transport in charge-neutral bilayer graphene. *Nat. Phys.* **13**, 1207–1214 (2017).
13. Moll, P. J. W., Kushwaha, P., Nandi, N., Schmidt, B. & Mackenzie, A. P. Evidence for hydrodynamic electron flow in PdCoO₂. *Science* **351**, 1061–1064 (2016).
14. Gooth, J. et al. Thermal and electrical signatures of a hydrodynamic electron fluid in tungsten diphosphide. *Nat. Commun.* **9**, 4093 (2018).
15. Braem, B. A. et al. Scanning gate microscopy in a viscous electron fluid. *Phys. Rev. B* **98**, 241304(R) (2018).
16. Sulpizio, J. A. et al. Visualizing Poiseuille flow of hydrodynamic electrons. *Nature* **576**, 75–79 (2019).
17. Narozhny, B. N. & Schütt, M. Magnetohydrodynamics in graphene: shear and Hall viscosities. *Phys. Rev. B* **100**, 035125 (2019).
18. Lucas, A., Crossno, J., Fong, K. C., Kim, P. & Sachdev, S. Transport in inhomogeneous quantum critical fluids and in the Dirac fluid in graphene. *Phys. Rev. B* **93**, 075426 (2016).
19. Lucas, A. & Fong, K. C. Hydrodynamics of electrons in graphene. *J. Phys. Condens. Matter* **30**, 053001 (2018).
20. Maze, J. R. et al. Nanoscale magnetic sensing with an individual electronic spin in diamond. *Nature* **455**, 644–647 (2008).
21. Roth, B. J., Sepulveda, N. G. & Wikswo, J. P. Using a magnetometer to image a two-dimensional current distribution. *J. Appl. Phys.* **65**, 361–372 (1989).
22. Zhou, T. X., Stöhr, R. J. & Yacoby, A. Scanning diamond NV center probes compatible with conventional AFM technology. *Appl. Phys. Lett.* **111**, 163106 (2017).
23. Maletinsky, P. et al. A robust scanning diamond sensor for nanoscale imaging with single nitrogen-vacancy centres. *Nat. Nanotechnol.* **7**, 320–324 (2012).
24. Pham, L. M. et al. Magnetic field imaging with nitrogen-vacancy ensembles. *New J. Phys.* **13**, 045021 (2011).
25. Xie, L., Zhou, T. X., Stöhr, R. J. & Yacoby, A. Crystallographic orientation dependent reactive ion etching in single crystal diamond. *Adv. Mater.* **30**, 1705501 (2018).
26. Kiselev, E. I. & Schmalian, J. Boundary conditions of viscous electron flow. *Phys. Rev. B* **99**, 035430 (2019).
27. Titov, M. et al. Giant magnetodrag in graphene at charge neutrality. *Phys. Rev. Lett.* **111**, 166601 (2013).
28. Alekseev, P. S. et al. Nonmonotonic magnetoresistance of a two-dimensional viscous electron–hole fluid in a confined geometry. *Phys. Rev. B* **97**, 085109 (2018).
29. Alekseev, P. S. et al. Counterflows in viscous electron–hole fluid. *Phys. Rev. B* **98**, 125111 (2018).
30. Cadore, A. R. et al. Thermally activated hysteresis in high quality graphene/h-BN devices. *Appl. Phys. Lett.* **108**, 233101 (2016).
31. Holder, T. et al. Ballistic and hydrodynamic magnetotransport in narrow channels. *Phys. Rev. B* **100**, 245305 (2019).
32. Cao, C. et al. Universal quantum viscosity in a unitary Fermi gas. *Science* **331**, 58–61 (2011).
33. Luzum, M. & Romatschke, P. Conformal relativistic viscous hydrodynamics: applications to RHIC results at $\sqrt{s_{NN}}$ = 200 GeV. *Phys. Rev. C* **78**, 034915 (2008).

Article

Methods

NV spin physics

An NV spin consists of a substitutional nitrogen atom and an adjacent vacancy in the diamond lattice. Its ground state is an $S = 1$ electronic spin-triplet with $m_s = 0, \pm1$ eigenstates, each with magnetic moment $m_s\gamma_e$, where $\gamma_e = 2.8$ MHz G^{-1} is the gyromagnetic ratio of the NV electronic spin. An NV spin can be initialized into the $m_s = 0$ state with optical excitation at around 532 nm wavelength. Optical excitation also generates spin-dependent photoluminescence in the 640–800 nm wavelength range, which allows optical spin readout. The $m_s = \pm1$ states are split from the $m_s = 0$ state by about 2.87 GHz at zero magnetic field, and are further split from each other at finite magnetic field due to the Zeeman effect.

Experiments employ electronic grade single crystal diamonds with a {100} front facet from Element Six, created using chemical vapour deposition. Atomic force microscopy ensures surface roughness is under 1 nm. Near-surface NV spins are created using ^{15}N implantation (Innovion) at 6 keV followed by annealing for both wide-field magnetic imaging and scanning probe magnetometry. This implantation energy generates NV spins at a depth of about 10–20 nm beneath the diamond surface. For wide-field magnetic imaging, a dosage [N] = 2×10^{12} cm^{-2} leads to an ensemble of [NV] $\approx 10^{11}$ cm^{-2}. For scanning probe magnetometry, a dosage is selected to ensure each probe contains on average one NV spin[22]. The diamonds are cleaned using a mixture of sulfuric, nitric and perchloric acids before deposition of van der Waals heterostructure or fabrication of scanning probe.

Device fabrication

To realize high-quality graphene devices, we generate a heterostructure of graphene and hBN[34]. A polymer-free assembly method[35] is used to prepare a van der Waals heterostructure for the devices. hBN and monolayer graphene (G) flakes are exfoliated on standard SiO$_2$/p-doped Si substrate. Polymer polycaprolactone[36] is used to pick up the flakes. For scanning measurement, three-layer hBN–G–hBN stacks are prepared on a standard substrate; the thickness ranges from 20 to 50 nm for the bottom hBN and from 10 to 20 nm for the top hBN. For wide-field magnetic imaging, a four-layer structure, consisting of an hBN-encapsulated graphene stack (top hBN 13 ± 1 nm thick and bottom hBN 27 ± 1 nm thick) together with a graphite top gate is deposited on a diamond.

Electron-beam lithography is performed using Elionix 7000 with 495 PMMA C6 as the resist. To mitigate charge build-up during fabrication of the graphene-on-diamond device, an additional layer of Aquasave is spun onto the diamond and conductive carbon tape is attached to the diamond edges. To pattern the stack and to make edge contacts, inductively coupled plasma reactive ion etch (RIE) with CHF$_3$ chemistry is employed (Surface Technology Systems). Electron-beam evaporation deposits 10 nm of chromium as an adhesion layer followed by gold of minimum 100-nm thickness for metallization and creation of other electrical structures (for example, microwave delivery for the graphene-on-diamond device and bond pads).

For the graphene-on-diamond device, it is necessary to create contact to the top gate graphite without shorting to the graphene. To accomplish this, first electron-beam lithography is used to write a dielectric structure with hydrogen silsesquioxane, which serves to insulate the top gate contact from the graphene. The top gate contact is then created. It is also necessary to ensure the top gate graphite is not shorted to graphene edge contacts. To accomplish this, graphite in the vicinity of the edge contacts is etched away using RIE with O$_2$ chemistry, which does not affect hBN.

Low-mobility graphene devices are prepared directly from exfoliated monolayer graphene flakes on SiO$_2$/p-doped Si substrate without hBN encapsulation. Furthermore, the samples do not undergo thermal annealing, in contrast to hBN-encapsulated devices. Instead of edge contacts, metallic electrodes are made directly on graphene without an RIE step before evaporating metals.

Wide-field magnetic imaging

The sample is positioned on a combined translational stage of Physik Instrumente M686.D64 for coarse positioning with about 0.1-µm precision, and P-541.2DD for fine positioning with roughly nanometre precision. NV centres are optically excited with a 532-nm laser (Coherent COMPASS 315M-100) switched on and off by an acousto-optic modulator (Isomet 1250C-974). The light is directed onto the sample with an Olympus 0.9NA ×100 objective. A Kohler-illumination system expands the laser beam to illuminate an area of about 5 µm in diameter on the sample. About 10 mW of excitation illuminates the sample. NV photoluminescence is collected by the same objective. The collected light passes through a 552-nm edge dichroic (Semrock LM01-552-25), after which it is separated from the excitation, passes through another 570-nm long-pass filter to further reduce light not in the photoluminescence wavelength range, and is imaged via a tube lens (focal length $f = 200$ mm) onto a camera (Basler acA1920-155um). The output of a microwave synthesizer (SRS SG384) is controlled by a switch (Mini-Circuits, ZASWA-2-50DR+), then amplified (Mini-Circuits, ZHL-16W-43-S+) and delivered onto the printed circuit board housing the sample. A permanent magnet, whose position is controlled by three sets of motorized translational stages (Thorlabs MTS25-Z8), is used to apply a uniform external magnetic field. A gate voltage is supplied by a Keithley 2420, and d.c. current for the measurement is supplied by a Keithley 6221.

Optically detected magnetic resonance (ODMR) spectra are measured by capturing an NV photoluminescence image at different microwave frequencies. The spectra contain both the $m_s = 0 \leftrightarrow -1$ (lower) and +1 (upper) resonances. To extract the resonance frequencies $f_\pm$, Lorentzian fits of photoluminescence versus frequency are performed at each pixel; the fitting function consists of a single Lorentzian or double Lorentzian if the ^{15}N hyperfine splitting is resolved. This procedure is applied with the external field (about 90 G) aligned along three of the four NV axes, labelled as $i = 1, 2, 3$. At each NV orientation, resonance frequencies for the upper transition $f_+(\pm I)$ and lower transition $f_-(\pm I)$ are recorded for current through the sample in the positive and negative polarity $\pm I$. At a given NV orientation, the projected stray field generated by the current can then be obtained as $B_\parallel = [(f_+(+I) - f_+(-I)) - (f_-(+I) - f_-(-I))]/(4\gamma_e)$. Determination of three projective field components $B_{\parallel,i}$ allow the vector magnetic field in the NV layer to be determined for all three Cartesian directions.

Four classes of orientations exist in the NV ensemble. Up to a rotation in the xy plane, the orientation vectors are given by

$$\hat{u}_{1,NV} = \frac{1}{\sqrt{3}}(\sqrt{2}, 0, 1) \tag{3}$$

$$\hat{u}_{2,NV} = \frac{1}{\sqrt{3}}(-\sqrt{2}, 0, 1) \tag{4}$$

$$\hat{u}_{3,NV} = \frac{1}{\sqrt{3}}(0, \sqrt{2}, 1) \tag{5}$$

$$\hat{u}_{4,NV} = \frac{1}{\sqrt{3}}(0, -\sqrt{2}, 1) \tag{6}$$

Here the coordinates are defined by the diamond, which we call the NV frame, (x_{NV}, y_{NV}, z). This differs from the coordinate in the device frame (x, y, z), which is such that the y direction is along the length of the channel, by a rotation of angle θ in the x–y plane. For a vector measurement, three projected fields are measured, $B_i = \mathbf{B} \cdot \hat{u}_{i,NV}$. Then, the vector field in the NV frame can be determined:

$$B_z = (\sqrt{3}/2)(B_1 + B_2) \tag{7}$$

$$B_{x,\mathrm{NV}} = \sqrt{3/2}\,(B_1 - B_2)/2 \tag{8}$$

$$B_{y,\mathrm{NV}} = \sqrt{3/2}\,(B_3 - B_z/\sqrt{3}) \tag{9}$$

The vector field in the device frame can be obtained by a rotation angle θ

$$\begin{pmatrix} B_x \\ B_y \end{pmatrix} = \begin{pmatrix} \cos\theta & -\sin\theta \\ \sin\theta & \cos\theta \end{pmatrix} \begin{pmatrix} B_{x,\mathrm{NV}} \\ B_{y,\mathrm{NV}} \end{pmatrix} \tag{10}$$

Current reconstruction is done using direct inversion of the Biot–Savart law in Fourier space

$$b_x(\mathbf{k}, d) = \frac{\mu_0}{2} e^{-d|\mathbf{k}|} j_y(\mathbf{k}) \tag{11}$$

$$b_y(\mathbf{k}, d) = -\frac{\mu_0}{2} e^{-d|\mathbf{k}|} j_x(\mathbf{k}) \tag{12}$$

where $b_{x,y}$ ($j_{x,y}$) are the Fourier transforms of the magnetic field $B_{x,y}$ (current density $J_{x,y}$), $\mathbf{k}$ is the wave vector, μ_0 is the vacuum permeability, and the stand-off distance (Supplementary Information) used is $d = 50 \pm 10$ nm. In this modality, uncertainty in the stand-off distance is the dominant source of error for the current density, which is about $9\ \mathrm{A\,m^{-1}}$.

Optical diffraction limits the point spread function of the wide-field magnetic imager, placing a Fourier low-pass filter on the current reconstruction, with a cut-off spatial frequency much lower than the cut-off placed by the NV layer stand-off distance (that is, the imager spatial resolution 420 nm is large compared with the stand-off $d \approx 50$ nm). Thus, high-spatial-frequency noise is suppressed by the wide-field magnetic imager and direct inversion of the device current is appropriate.

Scanning NV magnetic microscopy

The setup is described in ref. [23]. Scanning of the sample is performed with piezoelectric nanopositioners Attocube ANPxyz101 and ANSxyz100. The measurement pulse sequence is controlled by a Tektronic Arbitrary Waveform Generator (AWG) 5014C. Microwaves are supplied by a Rhode Schwartz SMB100A. As the device for scanning measurement is fabricated on a substrate with a global back gate, microwaves cannot be delivered on-chip as capacitive effects lead to poor microwave transmission. Instead, we use a separate antenna made from a wire of about 20-µm diameter placed about 50 µm above the device. The movement of the antenna is controlled by manual translational stages. The diamond probe consists of a nanopillar containing a single near-surface NV spin and is described in refs. [22,25].

A scanning measurement consists of iterating the piezovoltage V_x of the sample stage, and then performing OMDR or spin-echo magnetometry at each value of V_x. For a scanning ODMR measurement, current is supplied by a Keithley 2420. The ODMR measurement is performed in the same manner as in wide-field magnetic imaging, except that only one projection of $B_{||}$ is measured. For spin-echo a.c. magnetometry, a Hahn spin-echo $(\pi/2)_x - \tau - (\pi)_x - \tau - \pm(\pi/2)_{x,y}$ is employed. The first $(\pi/2)_x$ pulse generates an equal NV superposition state $(|0\rangle - i|-1\rangle)/\sqrt{2}$. A modulating square pulse of bias $\pm V_{\mathrm{a.c.}}$ is supplied to the graphene device from the AWG during the NV free precession time, generating a field of $\pm B_{\mathrm{a.c.}}$ on the NV. During the free precession, the NV picks up a total phase of $\phi = 2\gamma_e \tau B_{\mathrm{a.c.}}$. The NV is therefore in the superposition state $(|0\rangle + i e^{-i\phi}|-1\rangle)/\sqrt{2}$. The last $\pm(\pi/2)_{x,y}$ pulse leads to a photoluminescence (PL) readout signal of $\mathrm{PL}_{\pm x} = \mathrm{PL}_0 \pm A\cos(\phi)$ for $\pm(\pi/2)_x$ and $\mathrm{PL}_{\pm y} = \mathrm{PL}_0 - (\pm A\sin(\phi))$ for $\pm(\pi/2)_y$. Here, PL_0 and A are the average and half of the difference, respectively, of the photoluminescence signals of the $m_s = 0$ and the $m_s = -1$ states. Hence, $\mathrm{PL}_0 + A$ is the photoluminescence signal for the $m_s = 0$ state and $\mathrm{PL}_0 - A$ is the photoluminescence signal for the $m_s = -1$ state. Therefore, the NV phase can be determined as

$$\phi = \tan^{-1}\left(\frac{\mathrm{PL}_{-y} - \mathrm{PL}_{+y}}{\mathrm{PL}_{+x} - \mathrm{PL}_{-x}}\right) \tag{13}$$

The microwave pulses are tuned to the $m_s = 0 \leftrightarrow -1$ transition as determined via ODMR. Before the start of a scan, a spin-echo sequence is run without $V_{\mathrm{a.c.}}$ to determine the Hahn echo spin coherent time T_2, as well as locations of the NV spin coherence revival in the presence of the natural abundance ^{13}C bath. $\tau \approx 10$ or 20 µs is used. During a scan, the microwave drive Rabi frequency is measured at each spatial location to calibrate the microwave pulses. Spin-echo measurements are then performed with all four possible final microwave pulses $\pm(\pi/2)_{x,y}$ to obtain a measurement of the NV phase as described above. Differential measurements are also performed with the a.c. bias sequence $+V_{\mathrm{a.c.}}, -V_{\mathrm{a.c.}}$ and $-V_{\mathrm{a.c.}}, +V_{\mathrm{a.c.}}$, leading to a total of eight pulse-sequence combinations.

The current reconstruction for scanning NV microscopy is described in the Supplementary Information.

Transport measurement

Transport measurement of device conductivity σ is performed with a Stanford Research Systems lock-in amplifier (SRS SR830) at 17.77 Hz using a current-bias modality, with a large attached load of about 10 MΩ and source of about 100 nA. The gate voltage V_g is supplied by a Keithley 2420. Carrier density n is determined using $n = C_g(V_g - V_D)$, where V_D is the location of the CNP determined from location of the peak resistivity ρ, and $C_g = \varepsilon_0 \varepsilon_r/(et)$ is the gate capacitance per area, with ε_0 the permittivity of free space, ε_r the dielectric constant and t the thickness of the dielectric. For the graphene-on-diamond device, $\varepsilon_r = 4$ and $t = 13$ nm are used for the hBN gate dielectric. For the devices made on the standard SiO$_2$/Si substrates, $\varepsilon_r = 3.9$ and $t = 285$ nm are used.

Low-mobility graphene devices

The low-mobility graphene devices serving as a control are distinguished from standard, high-quality graphene devices in two ways: the absence of hBN-encapsulation and thermal annealing. It is known that such bare graphene devices without annealing are heavily doped, and are expected to have low mobility[37,38], with the CNP shifted to high gate voltage. The primary cause of strong disorder scattering in the low-mobility devices is twofold. First, the graphene is in direct contact with the SiO$_2$ substrate, which leads to scattering with charged surface states, impurities, surface roughness and SiO$_2$ surface optical phonons[34]. Second, the graphene is exposed to air and polymer used for lithography, leading to residue and contamination, which are known to act as external scattering centres and further limit the mobility[38,39]. Hence in these bare graphene devices, transport is dominated by disorder even at room temperature. We prepared two such devices, with optical images shown in Extended Data Fig. 1a, b. An example of the gate-dependent transport curve is shown in Extended Data Fig. 1c. From the slope of conductivity σ with respect to the gate voltage V_g, we extract the mobility as $\mu = (eC_g)^{-1}(d\sigma/dV_g)$, where C_g is the gate capacitance. We obtain $\mu \approx 1,000\ \mathrm{cm^2\,V^{-1}\,s^{-1}}$ for both devices, which is typical for such unannealed graphene in the literature and is close to two orders of magnitude lower than a typical hBN-encapsulated graphene device. Extended Data Fig. 1d is the same figure as Fig. 2e, but with (1) the palladium data removed and (2) the current profiles from both of the two low-mobility graphene devices displayed. We observe that in both low-mobility graphene devices, the current profile is sharp at the edges and flat within the channel, consistent with ohmic transport.

Article

Ruling out ballistic transport in encapsulated graphene device at room temperature

For a system of non-interacting ($\tau_{pp} = \infty$) electrons moving in a channel $-W/2 < x < W/2$ with a completely diffusive boundary, the flow profile is expected to develop a curvature in the regime where the momentum-relaxing mean free path is on the order of the channel width, $l_{mr} \sim W$. Therefore, it is important to rule out such ballistic transport as a possible explanation of the measured current profiles that display curvature. We performed such a check using two different approaches: (1) comparison of experimental profiles to calculated non-interacting (ballistic) current profiles and (2) magneto-transport measurements.

The derivation of non-interacting current profiles is described in the Supplementary Information. Comparison of a calculated non-interacting current profile with maximum curvature and an experimentally measured profile is shown in Fig. 2e. The spatial resolution and signal-to-noise of our experiment allows us to identify directly the transport regime based on the measured current profile in the graphene channel at the CNP. The observed profile smoothly decreases away from the centre of the channel and vanishes at the boundaries, within experimental uncertainty. A ballistic current profile has a discontinuity at the boundaries, which is inconsistent with our observation and is thus ruled out; whereas a viscous flow profile has a compelling match with the measured profiles.

The magneto-transport measurement is described in the Supplementary Information. With this technique, we find that while the device exhibits ballistic transport at 10 K, as expected given the device's high quality, ballistic transport is ruled out at room temperature.

Electron–hole recombination as possible source for higher-order feature in current profiles

With high-resolution scanning NV microscopy[22,25], we observe an isolated dip in the current profiles of the high-mobility graphene devices, close to the centre of the graphene channel (Fig. 2e, f). We note that recombination is expected to play a role in the transport of electron–hole systems[27–29] such as graphene at the CNP, leading to peaks in the current density associated with the edges of a flow in a channel[28,29]. This scenario is compatible with the scale of the recombination length in our devices, estimated to be about 1 μm in ref. [27], which is comparable to the channel width W. Furthermore, the dip is attenuated in one graphene device (the last profile on the right of Fig. 2f), which has higher carrier density inhomogeneity as indicated by a much broader density-dependent resistivity. We estimate a fluctuation potential of about 450–570 K for this device (Supplementary Information), which is substantial compared with the thermal energy and hence leads to an effective doping. The appearance of an attenuated dip in this device is also compatible with recombination leading to additional features in the current density, as recombination is exponentially suppressed upon doping.

Current profiles in wider channel of encapsulated graphene device

The shape of a current profile in the hydrodynamic regime, given by equation (1), depends on the ratio of D_v/W. In principle, changing the carrier density n may lead to changes in the kinematic viscosity v and the momentum-relaxing mean free path l_{mr}, and hence n may provide a means to tune the Gurzhi length $D_v = \sqrt{v l_{mr}}$ and thus the shape of the current profile. For example, scanning single-electron transistor measurements[16] in a 4.7-μm-wide graphene channel show that electron flow deviates from the ideal Poiseuille regime as n increases at $T = 75$ and 150 K. As shown in Fig. 4, in the standard 1-μm channel used in our encapsulated graphene devices, we observe qualitatively parabolic current profiles up to a carrier density of about 10^{12} cm^{-2}. We note that current profiles with $D_v/W > 0.3$ are indistinguishable within

experimental error bar; hence it is possible that variation in D_v due to changing n leads to insignificant change in the current profile in the standard 1-μm channel.

To investigate this scenario, we perform scanning NV microscopy in a wider channel, $W = 1.5$ μm, across a few different carrier density ranges. In Extended Data Fig. 2a, we show the current profile at the CNP. The profile is clearly flatter compared with the ideal Poiseuille limit. We can compare this profile in real space to the profile measured in the narrower 1-μm channel for the same device (Fig. 2e) by plotting the x axis in terms of micrometres (instead of the normalized unit x/W). In Extended Data Fig. 2b, we see that at the CNP, by moving from a narrower to a wider channel, a flatter profile is observed.

Next, we show a measured current profile in a regime slightly away from the CNP in Extended Data Fig. 2c. Here the density range is estimated to be $n = 0.08 \times 10^{12}$–0.30×10^{12} cm^{-2}. This profile is closer to a parabola. In a third density regime, estimated to be $n = 0.30 \times 10^{12}$–0.53×10^{12} cm^{-2}, the measured profile (Extended Data Fig. 2d) becomes flatter again. In these measurements, the density range is assessed in the same way as for the data shown in Fig. 4a (Supplementary Information).

This set of measurements shows that indeed, in a wider channel, the current profile is more sensitive to the carrier density variation. We find that at finite carrier density, further increasing the carrier density leads to the system moving away from the Poiseuille regime, which is consistent with the observation of ref. [16]. Near the CNP, we find that moving the system away from neutrality brings the system closer to the Poiseuille limit. In the regime of low carrier density and near the CNP, there is neither existing theory nor experiment to which our observations can be compared.

Here we comment on our observation in the context of the current understanding of the physics of graphene and carrier hydrodynamics. The shape of the current profile as a function of carrier density is expected to be determined by the n dependence of both v and l_{mr}. As found in ref. [5], v is rather insensitive to n at finite doping and near room temperature. However, it is known that l_{mr} near room temperature generally has a non-monotonic trend with n: increasing initially away from the CNP, and then decreasing as n continues to increase (see, for example, ref. [35]). This pattern has an intuitive explanation. At low carrier density, it is known that the lack of screening leads to contributions to momentum relaxation coming from disorder. Then, increasing density in this regime begins to screen disorder and hence reduces momentum relaxation. Once the system is at high carrier density, relaxation is limited by phonons[40] and l_{mr} decreases with increasing n. This non-monotonic behaviour of l_{mr} as a function of carrier density n may be related to the trend in current profiles observed here. Further theoretical and experimental work is needed to address this possibility.

Lastly, we note that while we observe current profiles in the wider channel that deviate from ideal Poiseuille behaviour, it is not appropriate to extract quantitative values for D_v from these profiles by fitting them to equation (1). A condition for hydrodynamics is that l_{mr} is not small compared with W. As $l_{mr} \approx 1$ μm near room temperature[35], equation (1) is less applicable for the wider channel. Consequentially, in the wider channel, the smaller l_{mr}/W ratio (that is, deviation from the hydrodynamic regime) can also lead to a flatter current profile. Therefore, in the wider channel, fitting the current profile to equation (1) is likely to extract a value of D_v that is smaller than the actual value.

Data availability

The data that support the plots and other analysis in this work are available upon request.

34. Dean, C. R. et al. Boron nitride substrates for high-quality graphene electronics. *Nat. Nanotechnol.* **5**, 722–726 (2010).
35. Wang, L. et al. One-dimensional electrical contact to a two-dimensional material. *Science* **342**, 614–617 (2013).

36. Son, S. et al. Strongly adhesive dry transfer technique for van der Waals heterostructure. Preprint at https://arxiv.org/abs/2006.15896 (2020).
37. Cheng, Z. et al. Toward intrinsic graphene surfaces: a systematic study on thermal annealing and wet-chemical treatment of SiO_2-supported graphene devices. *Nano Lett.* **11**, 767–771 (2011).
38. Moser, J., Barreiro, A. & Bachtold, A. Current-induced cleaning of graphene. *Appl. Phys. Lett.* **91**, 163513 (2007).
39. Lindvall, N., Kalabukhov, A. & Yurgens, A. Cleaning graphene using atomic force microscope. *J. Appl. Phys.* **111**, 064904 (2012).
40. Hwang, E. H. & Das Sarma, S. Acoustic phonon scattering limited carrier mobility in two-dimensional extrinsic graphene. *Phys. Rev. B* **77**, 115449 (2008).

Author contributions M.J.H.K., A.Y. and R.L.W. conceived the project. M.J.H.K., T.X.Z., A.Y. and R.L.W. designed the experiments. M.J.H.K. and T.X.Z. performed scanning NV measurements and room-temperature electrical transport measurements and analysed the data. T.X.Z. fabricated the scanning probes and built the scanning probe setup. M.J.H.K. and Q.L. built the NV wide-field imaging setup, performed the measurement, and analysed the data. M.J.H.K., T.X.Z., L.E.A., A.H. and U.V. performed the magneto-transport experiment and analysed the data. M.J.H.K., Y.J.S., J.K.S., C.B., A.T.P., Y.X. and H.Z. fabricated the devices. M.M.F. provided the theory on the current profile of non-interacting electrons. K.W. and T.T. grew the hBN single crystals. M.J.H.K., T.X.Z., Q.L., F.C., P.K., A.Y. and R.L.W. contributed to the discussion. M.J.H.K., T.X.Z., A.Y. and R.L.W. wrote the manuscript with input from all authors. P.K., A.Y. and R.L.W. supervised the project.
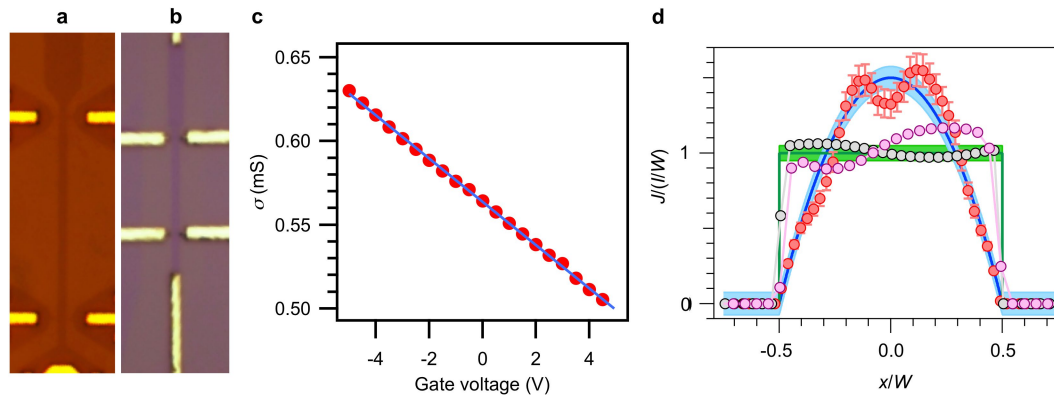
Article

Extended Data Fig. 1 | Low-mobility graphene devices. a, **b**, Optical image of the two bare monolayer graphene devices (**a** and **b**), with experimental results reported in panels **c** and **d**. The width of each device is $W = 1\,\mu m$. **c**, Conductivity σ as a function of the gate voltage V_g of the device shown in **a**. Data are shown in red. The blue line is a linear fit, which allows for extraction of the mobility. **d**, Current profiles of two bare monolayer graphene devices. Grey is for the device shown in **a**. Pink is for the device shown in **b**. The data are shown in comparison to the parabolic current profile measured for the encapsulated graphene device shown in Fig. 2e. Error bars correspond to the relative deviation of J_y that generates $2\chi^2$, where χ^2 is the cost function.
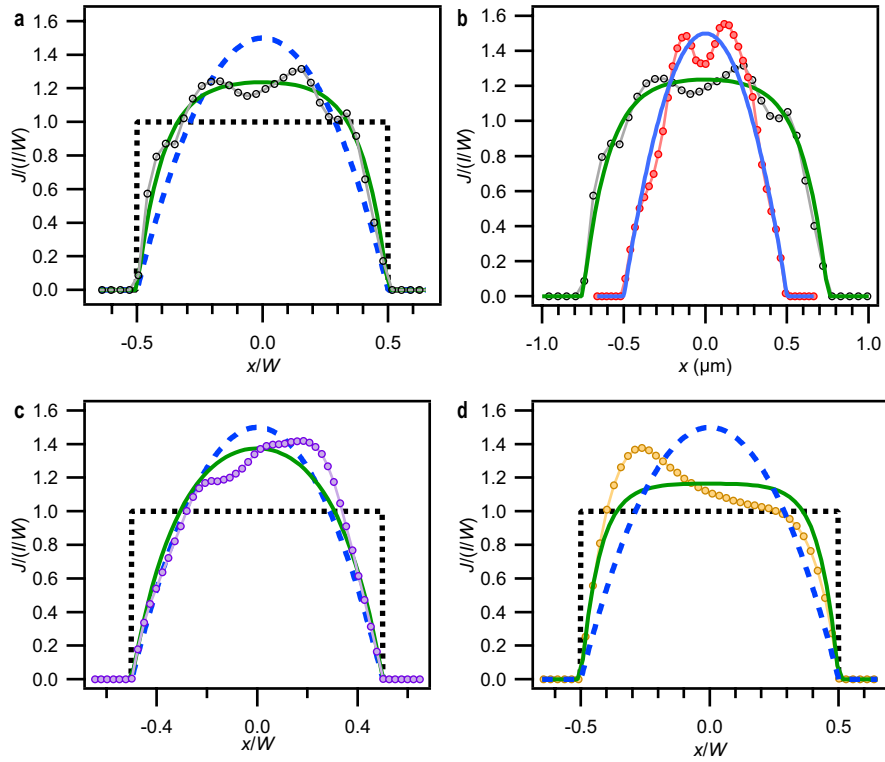
Extended Data Fig. 2 | Scanning NV measurement of current profiles in a $W = 1.5\,\mu m$ channel. a, Measurement at the CNP. **b**, Data from **a** compared with data from Fig. 2e. In this panel, the horizontal axis is x in micrometres, where for all the other panels the horizontal axis is x/W. **c**, **d**, Measurement in the estimated carrier density range $n = 0.08 \times 10^{12} - 0.30 \times 10^{12}\,cm^{-2}$ (**c**) and $n = 0.30 \times 10^{12} - 0.53 \times 10^{12}\,cm^{-2}$ (**d**). In **a**, **c** and **d**, the black dashed line is the ideal uniform profile, the blue dashed curve is the ideal Poiseuille profile and the green curve is a fit to the data with equation (1).